2-24-2014

Seismic and geodetic evidence for grounding-line control of Whillans Ice Stream stick-slip events

Martin J. Pratt

J. Paul Winberry

Douglas A. Wiens

Sridhar Anandakrishnan

Richard B. Alley

AGU PUBLICATIONS

JGR

Journal of Geophysical Research: Earth Surface

RESEARCH ARTICLE
10.1002/2013JF002842

Key Points:
- Ice stream seismic and GPS observations show grounding line control of motion
- GPS and seismic signals are combined, producing a high fidelity time series
- Teleseismic phases are radiated by ice stream sticky spots

Supporting Information:
- Readme
- Table S1
- Table S2
- Table S3
- Table S4
- Supp2
- Figure S2.1
- Figure S2.2
- Figure S3.1
- Figure S3.2
- Figure S4.1

Correspondence to:
M. J. Pratt,
martin@seismo.wustl.edu

Citation:
Pratt, M. J., J. P. Winberry, D. A. Wiens, S. Anandakrishnan, and R. B. Alley (2014), Seismic and geodetic evidence for grounding-line control of Whillans Ice Stream stick-slip events, *J. Geophys. Res. Earth Surf.*, *119*, 333–348, doi:10.1002/2013JF002842.

Received 30 APR 2013
Accepted 17 JAN 2014
Accepted article online 22 JAN 2014
Published online 24 FEB 2014

Seismic and geodetic evidence for grounding-line control of Whillans Ice Stream stick-slip events

Martin J. Pratt[1], J. Paul Winberry[2], Douglas A. Wiens[1], Sridhar Anandakrishnan[3], and Richard B. Alley[3]

[1]Department of Earth and Planetary Sciences, Washington University, St. Louis, Missouri, USA, [2]Department of Geological Sciences, Central Washington University, Ellensburg, Washington, USA, [3]Department of Geosciences, and Earth and Environmental Systems Institute, Pennsylvania State University, University Park, Pennsylvania, USA

Abstract The tidally modulated, stick-slip events of Whillans Ice Stream in West Antarctica produce seismic energy from three locations near the grounding line. Using ice velocity records obtained by combining time series from colocated broadband seismometers and GPS receivers installed on the ice stream during the 2010–2011 and 2011–2012 austral summers, along with far-field seismic recordings of elastic waves, we locate regions of high rupture velocity and stress drop. These regions, which are analogous to "asperities" in traditional seismic fault studies, are areas of elevated friction at the base of the ice stream. Slip events consistently initiate at one of two locations: near the center of the ice stream, where events associated with the Ross Sea high tide originate, or a grounding-line spot, where events associated with the Ross Sea low tide initiate, as well as occasional high-tide events following a skipped low-tide event. The grounding-line site, but not the central site, produces Rayleigh waves observable up to 1000 km away, through fast expansion of the slip area. Grounding-line initiation events also show strong directivity in the downstream direction, indicating initial rupture propagation at 1.5 km/s, compared to an average of 0.150 km/s for the entire slip event. Following slip initiation, additional seismic energy is produced from two sources located near the grounding line: first at the downstream end of Subglacial Lake Engelhardt and second toward the farthest downstream extent of the ice stream. This evidence suggests that the stronger, higher-friction material along the grounding line controls motion throughout the stick-slip region.

1. Introduction

Ice stream motion is important in determining ice sheet discharge. The mass balance of the West Antarctic Ice Sheet has been studied intensively over the last decade, showing negative mass balance in the Amundsen Sea region [e.g., *Pritchard et al.*, 2009] and positive mass balance along the Siple Coast [*Joughin and Tulaczyk*, 2002; *Chen et al.*, 2009]. The life cycle of the Siple Coast ice streams appears to alternate between times of fast, smooth motion (e.g., MacAyeal and Bindschadler Ice Streams) and times of stagnation (Kamb Ice Stream) [*Bennet*, 2003; *Clarke*, 2005; *Hulbe and Fahnestock* 2007]. The Whillans Ice Stream (WIS, formerly Ice Stream B) is slowing at a rate of 0.6%/yr^2 [*Joughin et al.*, 2005] and may be in the process of stagnating. More recent measurements show that the lower region of WIS has been decelerating at ~10 m/yr^2 since 2004 [*Winberry et al.*, 2013a, 2013b]. However, the mechanical controls on the temporal variability of ice stream motion are poorly understood and are the subject of vigorous investigation [*Winberry et al.*, 2009, 2011; *Walter et al.*, 2011].

The lower part of WIS, an 8000 km^2 ice plain of very low basal and surface slope, displays stick-slip motion modulated by the Ross Sea tide [*Bindschadler et al.*, 2003; *Winberry et al.*, 2009] (Figures 1 and 2a). Elastic strain, built up between slips, is released approximately twice daily during a 20 to 30 min long period of motion that accounts for most of the ice stream displacement [*Winberry et al.*, 2011]. Each slip event releases seismic energy observable more than 1000 km away, primarily as two or three surface-wave packets in the 30 to 100 s frequency band [*Wiens et al.*, 2008] and with microseismicity observed on the ice stream [*Winberry et al.*, 2013a, 2013b]. These stick-slip events offer an excellent opportunity to study the factors controlling friction and resistance along the base of an ice stream.

The coherent motion of the extensive, massive trunk of WIS produces seismic radiation during slip events, dominated by low-frequency, 30–100 s surface waves. The seismic energy is distinctly different from the generally much smaller, higher-frequency events produced beneath a wide range of glaciers from localized

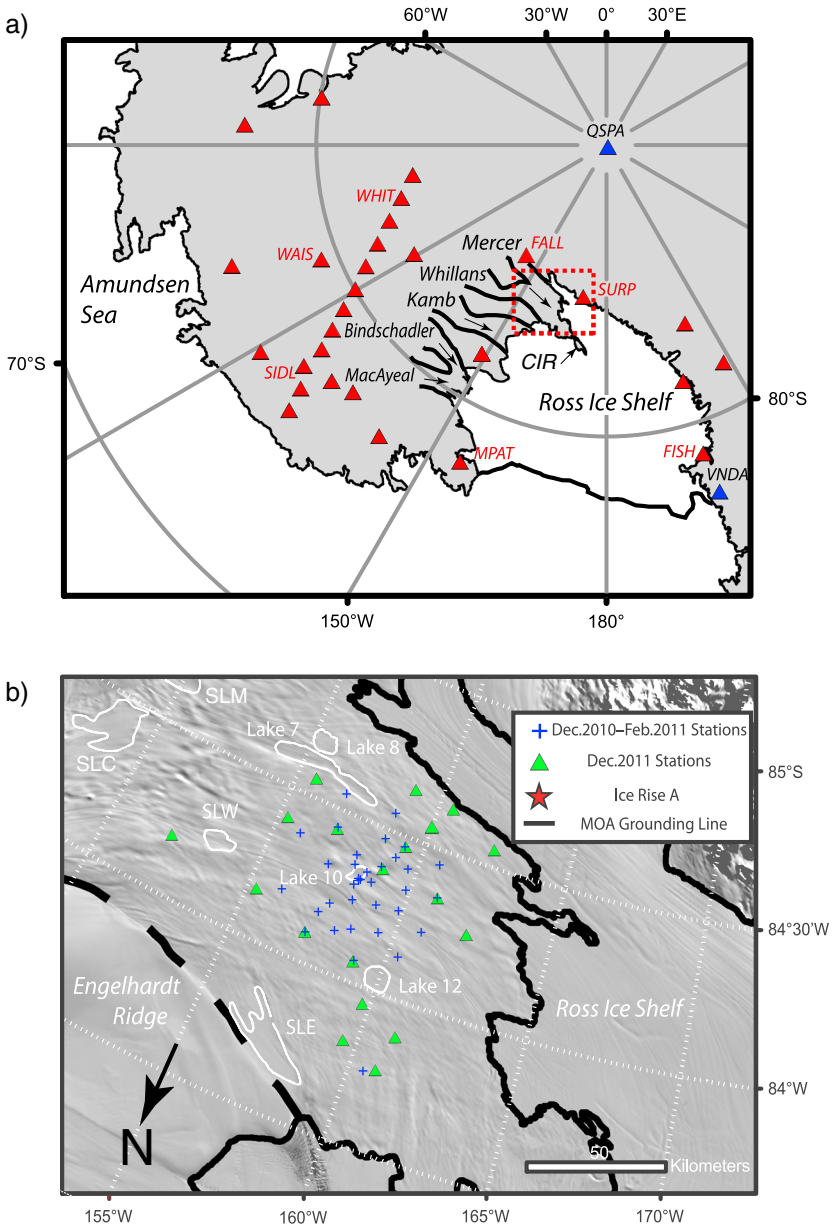

Figure 1. (a) Seismic station coverage in West Antarctica during our on-ice deployments. Red triangles are locations of POLENET/ANET stations, and blue triangles are GSN stations. Black lines mark boundaries of the Siple Coast ice streams with arrows showing direction of flow. Red box marks location of Figure 1b. CIR = Crary Ice Rise. (b) WIS array station location map. Grounding line and background image from Moderate Resolution Imaging Spectroradiometer (MODIS) Mosaic of Antarctica (MOA) [*Scambos et al.*, 2007]; subglacial lakes (white outlines) [*Fricker and Scambos*, 2009] SLE = Subglacial Lake Engelhardt, SLW = Subglacial Lake Whillans; and northern shear margin (white dashed line).

asperities [*Blankenship et al.*, 1987; *Anandakrishnan and Bentley*, 1993; *Zoet et al.*, 2012a, 2012b]. Ice-calving events have been shown to produce surface waves at periods greater than 30 s [*Ekström et al.*, 2003; *Nettles and Ekström*, 2010]; however, the origins of these WIS signals are 600 km away from the nearest calving front, ruling out this source type. Based on the GPS data from 2003–2004, *Wiens et al.* [2008] suggested that the source location of the initiation of rupture, believed to be the cause of the first seismic phase, was a topographical feature known in the literature as Ice Rise A in the center of the ice stream (although this feature is not an ice rise, for continuity it will be referred to as such). The subsequent surface-wave origins after slip initiation were not well constrained by the *Wiens et al.* [2008] study. *Walter et al.* [2011] used data collected in 2008 to suggest that slip did not start at Ice Rise A but closer to the southern edge grounding line near the

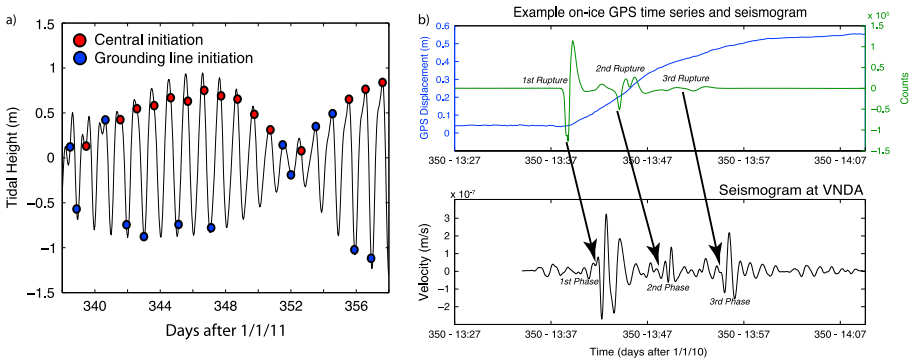

Figure 2. (a) Slip event times and types. Note that missed low-tide events are now more common than low-tide slips. Ross Sea tide (black) is CATs2008a tidal model (L. Padman, personal communication, 2008). (b) Example on-ice colocated GPS (blue) and raw seismogram (green—instrument response not removed) and the correlation with 30–100 s filtered vertical-component seismogram at VNDA showing the relationship of in situ translational velocity changes and far-field seismic phases.

suture between Mercer and Whillans Ice Streams. However, seismic stations used during that deployment were located upstream of the majority of stick-slip moving ice and so did not provide a precise position for slip initiation. Additionally, rupture velocity estimates were based on the time between each surface-wave arrival, which only allows for calculation of average rupture velocity and not localized variations.

Wiens et al. [2008] proposed that the initial seismic phase resulted from strong seismic radiation from a region of high friction and thus high stress along the base of the ice stream similar to an "asperity" in the seismological literature [*Das and Aki*, 1977; *Lay and Kanamori*, 1981]. Patches of higher friction at the base of glaciers and ice streams are often termed "sticky spots" in glaciology [e.g., *Alley*, 1993; *Sergienko and Hulbe*, 2011], and on WIS these regions appear to be analogous to asperities. *Wiens et al.* [2008] further proposed that the second and third seismic phases represented stopping phases caused by the rapid decrease in moment rate as the rupture moved off the land to the floating ice. However, *Winberry et al.* [2011] found that the second seismic phase corresponded to a later increase in rupture velocity and area associated with a second region at the northern edge of the ice stream.

In this study, we use data gathered from instruments placed in situ on WIS during the 2010–2011 and 2011–2012 austral summers, together with far-field seismograms from the Polar Earth Observing Network/Antarctic Network (POLENET/ANET) seismic array [*Wilson et al.*, 2010] and Global Seismic Network (GSN) stations (Figure 1), to constrain the dynamics of the slip events. The use of colocated seismographs and GPS receivers allows us to produce high-fidelity (0–10 Hz) broadband records of ice velocity by combining the GPS signal, which has better resolution at very low frequencies, with seismic velocity records providing better resolution at higher frequency. The use of seismometers allows us to pick the onset of motion at each location with increased accuracy and to be able to monitor the progression of slip rupture in more detail than is possible from GPS alone. The results allow us to more accurately resolve the locations of the rupture origins and to demonstrate that most of these regions are located along the grounding line. This evidence suggests that the WIS grounding line represents a strong region of higher resistance and may be controlling the dynamics of WIS. One particular goal of this study is to understand how WIS rupture produces the features of the far-field waveforms, so that the time evolution of tidally modulated WIS slip events can be tracked in the past and potentially in the future during times when there are no sensors directly on the ice stream. Increased azimuthal coverage of seismic stations around WIS in West Antarctica now has the ability to observe variations in the waveforms that can provide seismic source parameter information.

2. Data

We present two types of data in this study and a variety of analysis methods. Each methodology will be described with each set of results.

First, section 3 describes results from data collected by GPS and seismic sensors located in situ on WIS. Field deployments on WIS were carried out during December 2010 to January 2011 and December 2011.

Instruments were more closely spaced than in the previous deployments [*Wiens et al*., 2008; *Winberry et al*., 2009; *Walter et al*., 2011] to give better resolution of the onset locations. During each season, in situ seismographs were deployed on WIS, with GPS colocated at many of the sites.

For the 2010–2011 field season we deployed a dense, circular array of 17 Trillium-120PA and 18 Guralp 40 T broadband sensors (Figure 1b) around the previously estimated slip origin point of *Wiens et al*. [2008] (Ice Rise A) with an aperture of 60 km; 20 stations were colocated with geodetic-quality GPS receivers. The seismic sampling rate was 200 Hz, and the GPS sampling rate was 0.067 Hz. Seismic sensors were buried 50 cm beneath the surface, with each colocated GPS station situated less than 10 m away.

During the second season, December 2011, stations were installed in a more widespread array of 14 Trillium-120PA broadband seismometers sampling at 500 Hz and 16 GPS (Figure 1b) sampling at 0.067 Hz. Eleven stations were colocated with GPS and seismic sensors. At seven locations, we reoccupied sites from the 2003–2004 Tidal Modulation of Ice Stream Flow (TIDES) experiment with GPS recorders. The arrangement of array stations was based on preliminary results from the 2010–2011 array.

Second, methods described in section 4 use far-field data to study variations in propagating elastic surface waves generated by WIS. Data are used from broadband seismographs at distances of 140–1250 km in Antarctica to provide additional constraints on the slip characteristics of WIS (Figure 1). Regions of rapid rupture expansion produce propagating surface-wave packets that can be detected at far-field seismographs [*Wiens et al*., 2008]. Teleseismic coverage has increased in recent years with the introduction of the POLENET/ANET array throughout West Antarctica [*Wilson et al*., 2010]. For the far-field study we use data from 26 POLENET/ANET stations and two permanent Global Seismic Network stations, VNDA (Vanda Dry Valley) and QSPA (South Pole). The highest-amplitude signals observed at QSPA are Love waves on the horizontal component, consistent with the energy radiation patterns of Rayleigh and Love waves for a near-horizontal fault close to the Earth's surface [*Ben-Menahem and Singh*, 1981; *Wiens et al*., 2008]. The ability to study radiated surface waves at an increasing number of azimuthal directions leads to better constraints on the locations and characteristics of the sources. Section 4.4 presents a way of relating the in situ to the far-field observations and explains some of the variation in surface-wave amplitude.

3. In Situ Observation of Whillans Ice Stream Stick-Slip Motion

3.1. In Situ GPS and Seismic Data

While seismographs are typically deployed to record elastic deformation associated with the passing of seismic waves, the 2004 Tidal Modulation of Ice Stream Flow (TIDES) geophysical data indicated that broadband seismographs are recording relative velocity changes and are detecting the higher-frequency ($>$0.01 Hz) components of the translational ice motion (see also *Walter et al*. [2011]). With these time series, the propagation of the rupture front dominates the signal on both the GPS instruments and seismometers. Thus, horizontal-component seismographs provide a superior record of the details of the ice slip events, whereas standard GPS receivers provide precise measurements of the permanent offsets caused by the slip events. With the flow direction of WIS being ~290°, the amplitude is an order of magnitude larger on the east-west component than on the north-south component.

The seismographs deployed on WIS record three separate pulses of abrupt ice velocity change during a slip event, each corresponding to the passage of a rupture front. These three rupture signals correlate temporally, when corrected for traveltime, with distinct surface-wave arrivals observed in the far-field in the 30 to 100 s frequency band [*Wiens et al*., 2008] (Figure 2b). This demonstrates that each of the far-field surface-wave arrivals is radiated by a coincident pulse of higher-velocity ice movement, most likely due to a localized increase in rupture velocity, identified by the in situ observations. The new dense array of geodetic observations also reveals that prior to the first pulse of fast slip ($>$15 m/d) and associated rupture across the ice stream, 10–20 min of slow slip (5–10 m/d) is observed in the nucleation region [*Winberry et al*., 2013a, 2013b]. Additionally, the new results show that during 2010–2011, low-tide slip events were often skipped (out of 19 low tides during the deployment, 10 of these periods did not produce slip), whereas skips were infrequent in earlier observations from 2003 to 2004 (~1% of days) (Figure 2a) [*Winberry et al*., 2009]. The increased frequency of these skipped slips is likely related to the ongoing deceleration of the WIS and is the focus of another manuscript.

3.2. Location of Rupture Onset and Slip Phases via Beamforming

On-ice horizontal seismometer records display sudden increases in translational ice velocity associated with the onsets of each of the three rupture fronts during a slip event (Figure 2b). We exploit these seismometer records of ice motion to track the onset of the rupture front, since the onsets are not well recorded on the GPS data due to noise at higher frequencies (periods $<$300 s).

We use the traditional array method of spherical beamforming analysis to isolate the location from where these rupture fronts originate as well as their propagation velocity. Spherical beamforming of propagating pulses can be used to calculate the source location in an isotropic medium:

$$x_i(t) = f(t - \mathbf{r}_i \cdot \mathbf{u}_{\mathrm{hor}}) + n_i(t) \quad (1)$$

where $x_i(t)$ is the delayed ith component trace, $f(t)$ is the original seismogram, $\mathbf{r}_i$ is the location vector of stations i, $\mathbf{u}_{\mathrm{hor}}$ is the horizontal slowness of the propagating pulse in all directions, and $n_i(t)$ is a noise factor that is station specific [*Rost and Thomas*, 2002, equation (5)]. Here we apply the same delay-and-sum technique in the time domain to translational ice motion signals observed at seismic stations in close proximity to the source location using the E-W component to mitigate the influence of spatial variations in rupture propagation. We find the maximum coherency between the array of stations by searching all possible source locations using a grid spacing of 0.05° of latitude between 83.21° and 86°S, 0.25° of longitude between 150°W and 170°. We test a range of rupture velocities between 0.9 to 1.6 km/s. Maximum coherencies were obtained for velocities exceeding 1 km/s with maximum values of 1.2 km/s obtained. These estimates are faster than those of previous studies but confirmed by plane-wave frequency-wave number analysis (see supporting information section S2).

These results indicate that rupture begins at one of two separate initiation locations. Typical high-tide events show a maximum power at 84.4°S, 157°W near the center of the stick-slip region (Figure 3a). To highlight the suitability of our method, this calculation was done without including the station that records the first indication of motion, with the results showing a strong correspondence between peak power and the location of initial motion. A maximum power for typical low-tide events indicates that ruptures start at the south of the array at a location of 84.55°S, 163°W, close to or on the grounding line (Figure 3b).

The GPS closest to the central initiation location shows almost no motion between events, whereas the GPS closest to the grounding-line initiation location shows slow interevent motion. The grounding-line location can be termed a "slipping asperity," in contrast to the interevent-locked central asperity.

The second and third accelerations, in response to two further asperities breaking, begin at or close to the grounding line farther downstream between the Engelhardt Ice Ridge and Crary Ice Rise (Figure 1b). Initiation of the second rupture occurs at the downstream end of Subglacial Lake Engelhardt at 83.6°S, 159°W, where the grounding line is close to the edge of the lake (Figure 3c). The resolution of these data is insufficient to show whether the rupture starts from the grounding line, the edge of the lake, or somewhere between. It seems likely that during the loading between slip events stress is localized on this small region of grounded ice (~30 km^2) between Subglacial Lake Engelhardt and the Ross Sea, making it particularly susceptible to rupture when triggered by the onset of the distal part of the first rupture. The location of initiation of the third rupture acceleration is less well resolved due to lack of stations on the downstream end of WIS (Figure 3d). We do, however, find that the propagating pulse from the source has the same polarity (first motion down on the E-W component, consistent with an increase in westward ice flow velocity) as the first and second rupture fronts (Figure 2b), which indicates a further acceleration and not a stopping phase. Unlike the spatial variability of the onset rupture pulses, we find that the second and third rupture initiation locations do not change measurably between events.

3.3. Rupture Propagation

Following initiation of a slip phase, the propagation of the rupture across the ice stream can be tracked by using the seismometer record of ice motion. Rupture propagation is similar for slip events of similar duration, allowing us to combine data from both the 2010–2011 and December 2011 deployments to provide higher resolution of rupture front expansion. Traveltime picks from stations are recorded if a rupture signal is observed, and only those stations are used for interpolating the isochrones.

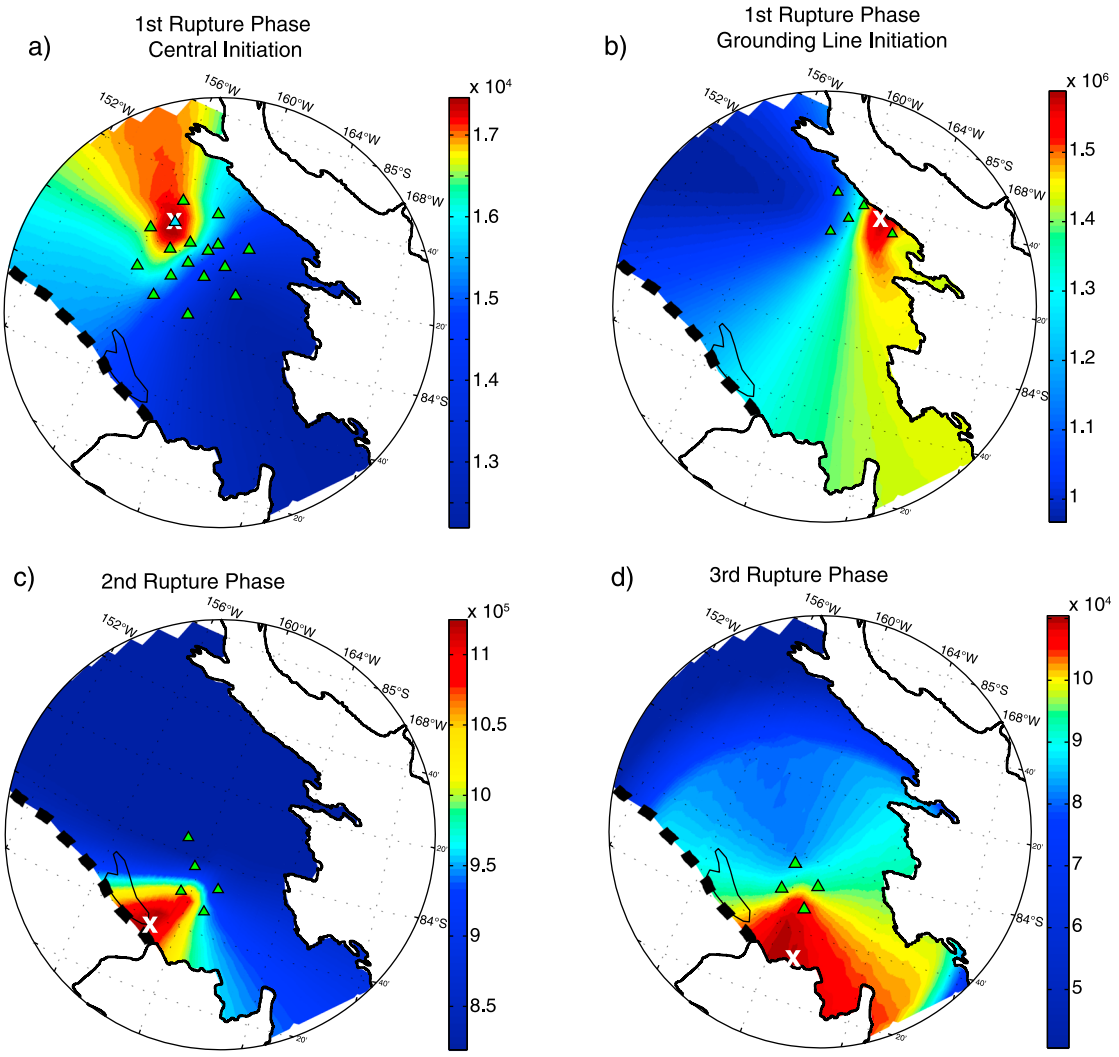

Figure 3. Beamformed locations where scale is power of stack (counts). (a) Central initiation location, rupture velocity: 1 km/s. Blue triangle signifies the station where rupture is first observed; this station was not used in the beamforming analysis. (b) Grounding-line initiation, rupture velocity: 1.4 km/s. (c) Second-rupture source, rupture velocity: 1.4 km/s. (d) Third-rupture source, rupture velocity: 1 km/s. White cross signifies maximum amplitude of beamed seismograms. Stations used (green triangles), MOA grounding line, SLE (Subglacial Lake Engelhardt), and northern shear margin (dashed line) are also marked.

Initial rupture velocity is slower for the central initiation asperity events than for grounding-line initiation events. Both appear to show anisotropic rupture, with faster propagation along flow than across flow, and a suggestion of faster propagation downstream than upstream (i.e., not propagating at equal velocity in all directions). However, rupture anisotropy is less well observed for grounding-line initiation events due to the source location being on the edge of the array (Figures 4a and 4b). And for both styles of onset, the rupture velocity decelerates as it moves away from the source (shown in Figure 4 as tighter isochrone contours farther away from the source location). This deceleration occurs as the rupture front propagates into regions where interevent strain accumulation is reduced [*Winberry et al.*, 2011].

Initiation of the second rupture event, on the downstream section of WIS, accelerates parts of the ice stream that are already in motion from the initial rupture. As a result, this rupture front is seen to propagate across the entire ice stream from its source close to the downstream end of Subglacial Lake Engelhardt (Figure 4c). Acceleration of slip is observed on parts of the ice stream already in motion that have yet to completely release strain accumulated between slip events (Figure 4d). The zone of this reacceleration from the second rupture front is spatially limited; farther away, at the southern edge of WIS, the second rupture front slows ice stream deceleration without reversing it. The third rupture front initiation has a similar effect on velocities in

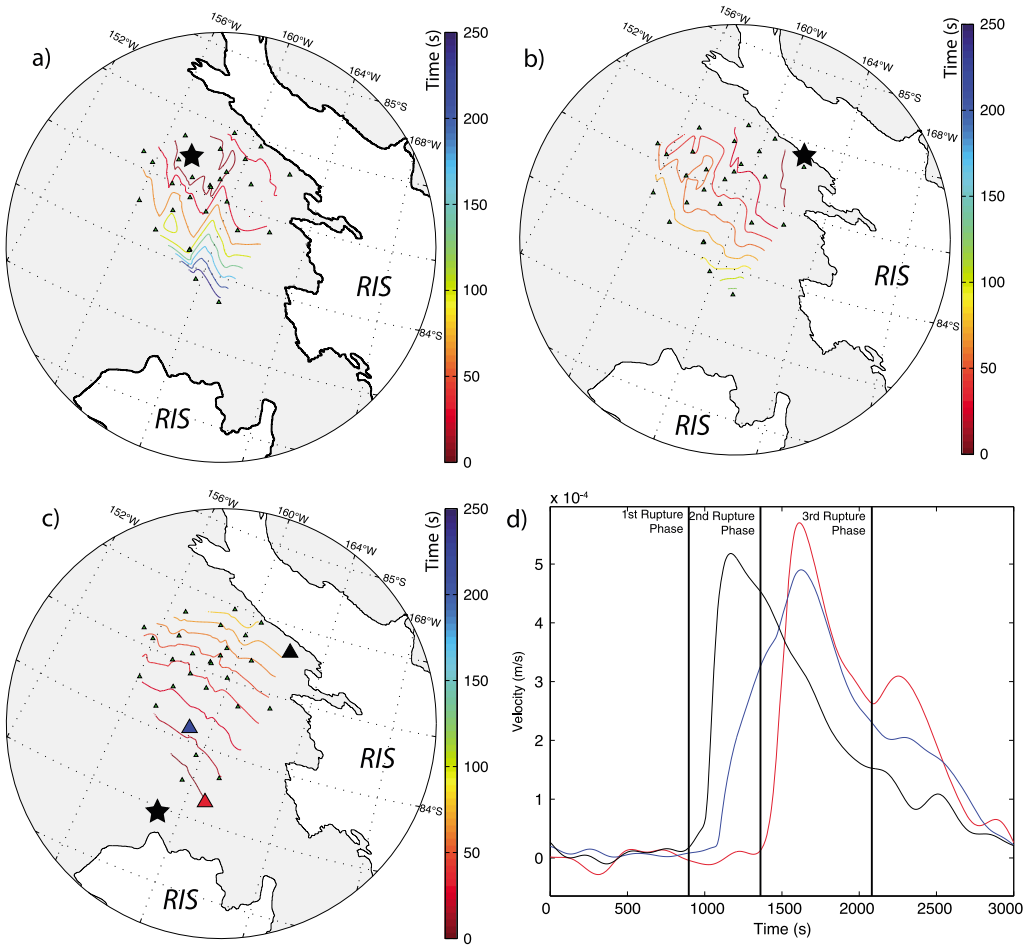

Figure 4. Rupture patterns using combined 2010 and 2011 traveltime pick data. The first rupture phase is recorded at all stations but two of the most downstream, whereas the second rupture phase is recorded at all stations. Similar slip events from both field seasons using duration and onset location were combined to show rupture propagation with isochrone contours for (a) central initiation, (b) grounding-line initiation, and (c) second-phase initiation. RIS = Ross Ice Shelf; black stars show acceleration initiation locations. (d) Broadband velocity functions formed by combining GPS and seismograph records for three stations across the array. Colors correspond to stations shown in Figure 4c. Vertical black lines show the onsets of accelerations that correspond to the teleseismic phases.

sections of the ice stream that are already moving, but over a smaller area, in the most downstream portions of WIS (Figure 4d).

4. Far-Field Seismic Signatures of Whillans Ice Stream Stick-Slip Events

4.1. Tidal Modulation of Waveform Characteristics

The on-ice studies show that there are four categories of WIS slip events (supporting information Table S4), each with a characteristic and repeatable temporal and spatial slip pattern and subsequent teleseismic waveform. The on-ice rupture and far-field waveform characteristics depend on whether the WIS slip events occur near Ross Sea high tide or low tide and whether they occur after a slip event fails to occur at its normal time (skips). We categorize these four observed types of slip event:

1. Typical high-tide slips, for which fast rupture initiates from the interevent-locked central asperity (Figure 5a). These occur shortly after high tide, as has been observed during temporary deployments over the last 10 years [*Bindschadler et al.*, 2003; *Walter et al.*, 2011].
2. Typical low-tide slips, for which fast rupture initiates from the slipping grounding-line asperity (Figure 5b). In 2010–2011 these were skipped much more often than in 2003–2004 [*Winberry et al.*, 2009], suggesting that these slip events are increasingly skipped due to the longer-term slowdown of WIS.

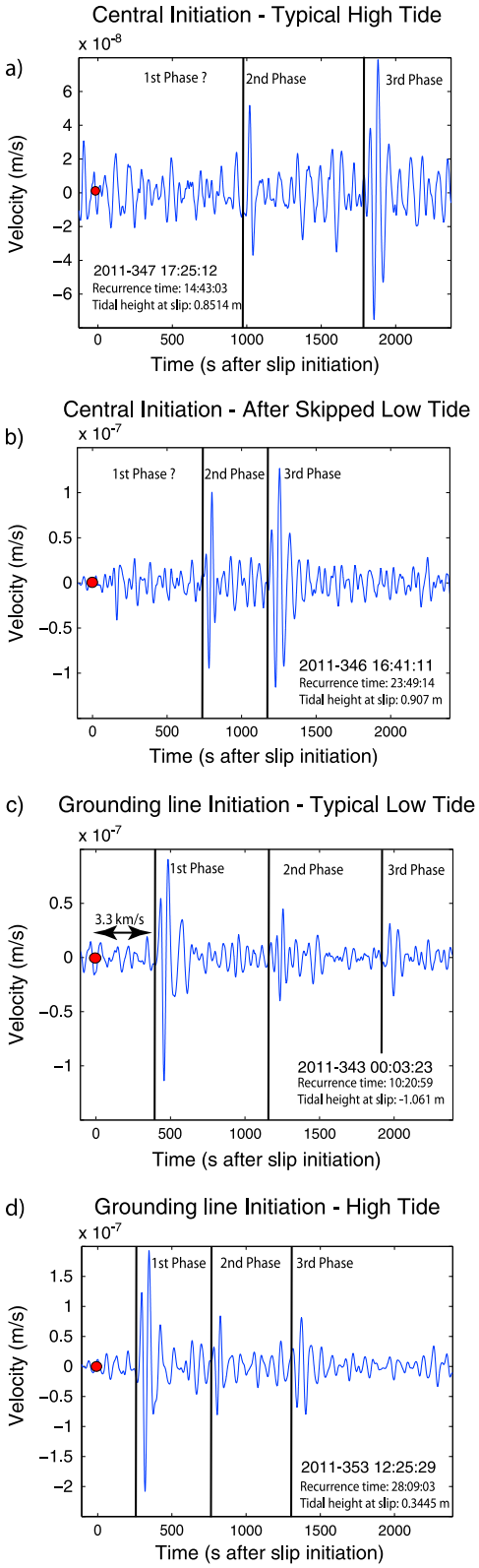

3. High-tide slips after low-tide skips, which have the same central initiation site as normal high-tide slips (Figure 5c). These events show larger total slip due to the long recurrence interval (>20 h), as well as faster rupture propagation and stronger teleseismic amplitudes compared to normal high-tide events.
4. High-tide slips initiating from the grounding-line asperity where normally low-tide slips start (Figure 5d). These occurred once or twice per spring-neap tidal cycle in 2010–2011, usually near neap tide prior to the high tide reaching 0.5 m above its mean and after a recurrence time in excess of 15 h. These slips are generally the most energetic, emitting signals recorded with the best signal-to-noise ratio, and have total durations less than 20 min due to their high rupture velocity. An event similar to these occurred on 25 January 1999 [*Bindschadler et al.*, 2003], suggesting that while these types of events may now be more frequent, they are not a recently developed phenomenon.

A far-field Rayleigh arrival corresponding to the initial rupture onset is seen clearly only when the event initiates at the grounding-line asperity. Rupturing of the central asperity generally produces no discernible vertical-component far-field response above the ambient noise level. Second- and third-phase signals are observed during all slip events. The far-field signature of high-tide events is heavily influenced by the interevent recurrence time, with higher amplitude but shorter duration resulting from faster rupture following skipped low-tide events. During neap tides (<0.4 m either side of mean sea level) the tide modulates slip to a lesser degree. As such the ice stream tends to initiate slip at only the central initiation spot during these periods, as the grounding-line spot cannot be loaded fast enough to fail first.

4.2. Teleseismic Locations of the Second and Third Slip Phases

Three packets of Rayleigh waves can be observed on many of the POLENET stations for each WIS slip event initiating from the grounding-line asperity (see supporting information Figure S3.2). Small differences in the arrival times of the Rayleigh waves at different azimuths place constraints on the relative locations of the source region

Figure 5. Variations in teleseismic vertical-component waveforms at station VNDA at a distance of 980 km. (a and b) Central initiation lacks first-phase Rayleigh wave arrival, whereas (c and d) grounding-line initiation shows a strong signal. Note the change in amplitude and total duration with recurrence time. Red circles indicate origin times determined by on-ice seismogram picks. Recurrence time is defined as the time since the onset of the previous slip; tidal height is determined from the CATs2008a model (L. Padman, personal communication, 2008); group velocity of Rayleigh waves shown in Figure 5c.

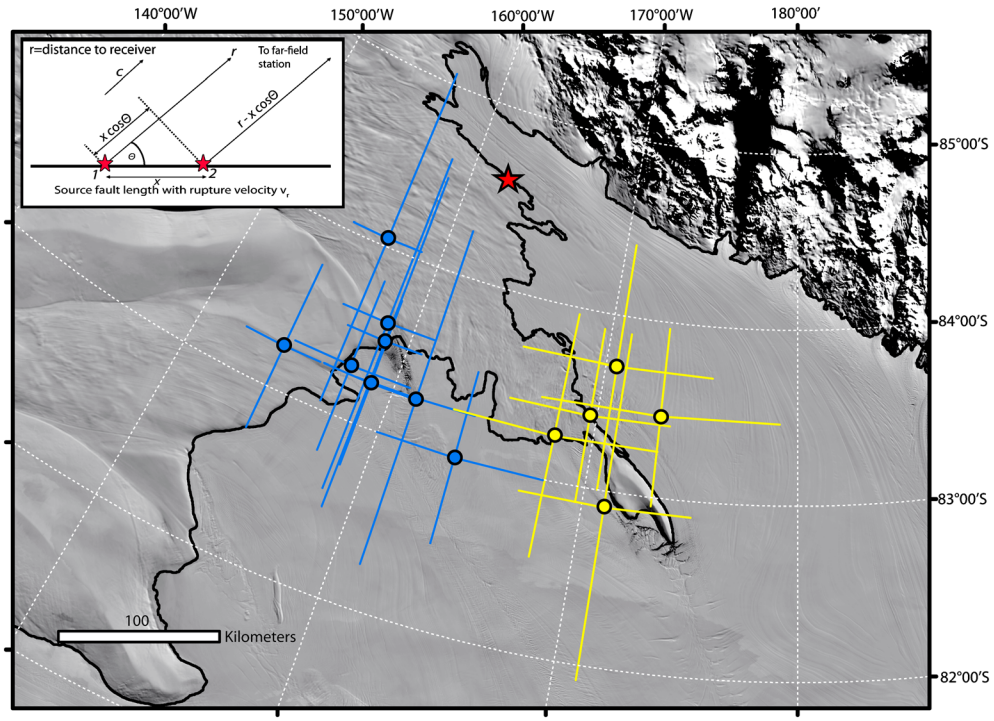

Figure 6. Seismic source locations of low-tide events calculated from relative traveltimes from POLENET/ANET stations. The initiation location of the first phase (red star) is from beamforming results (84°36′43″ 161°57′50″W). Blue and yellow circles correspond to minimum residual times of a grid search for second and third-phase relative arrival times. Gaussian noise simulation error bars for one standard deviation at 15 s are shown. (inset) Schematic illustration to show the formulation of equation (2) (adapted from *Lay and Wallace* [1995]).

for each of the packets. The arrival times of the first Rayleigh packet show that it is radiated by the initial rupture of the grounding-line asperity. We can therefore find the source locations of the second and third slip phases by constraining the first phase to the in situ determined onset location. Sources are located using a geometric inversion of relative traveltime delays of the second- and third-phase arrivals relative to the first (τ):

$$\tau = \frac{x}{v_r} - \left(\frac{x\cos\Theta}{c}\right) \tag{2}$$

where x is the distance between sources, v_r is the rupture velocity, c is the surface-wave velocity, and θ the azimuth between the fault direction and the receiver at the initial source (Figure 6). We minimize x/v_r to calculate the least-squares best fit solution for x and θ. In doing so we remove the dependency on knowing the rupture velocity, which varies between slip events, to calculate the source location. Using a relative location technique reduces errors associated with velocity heterogeneity along the paths, as all observations at a given station have similar far-field paths. Slip events initiating from the central asperity were not used since no far-field first-phase signals are observed. Given that picking traveltimes for surface waves in this frequency band is inherently ambiguous, a pick cutoff error of ±15 s is implemented. A Gaussian noise simulation is applied to analyze the goodness of fit for each location. Random noise with a standard deviation of 15 s is applied to the traveltime picks, and errors are calculated at the 68th percentile.

The source locations determined in this way for each seismic phase cluster on a separate part of the ice stream (Figure 6) but provide no definitive location. The second-phase cluster is toward the northern edge of the ice stream in the vicinity of Subglacial Lake Engelhardt. Third-phase signals proved to be less well observed in the far-field reducing the number of events available for analysis. However, the general location of the third phase in the downstream region is consistent with downstream locations found for this pulse by *Wiens et al*. [2008] and roughly correlates with the location of the final asperity observed by the in situ arrays.

4.3. Moment Rate Function: Combining GPS and Seismic Time Series of Ice Motion

The above correlation of far-field arrivals with the rupture of specific asperities leaves several questions unanswered. For example, why does rupture of the slipping grounding-line initial asperity produce a far-field

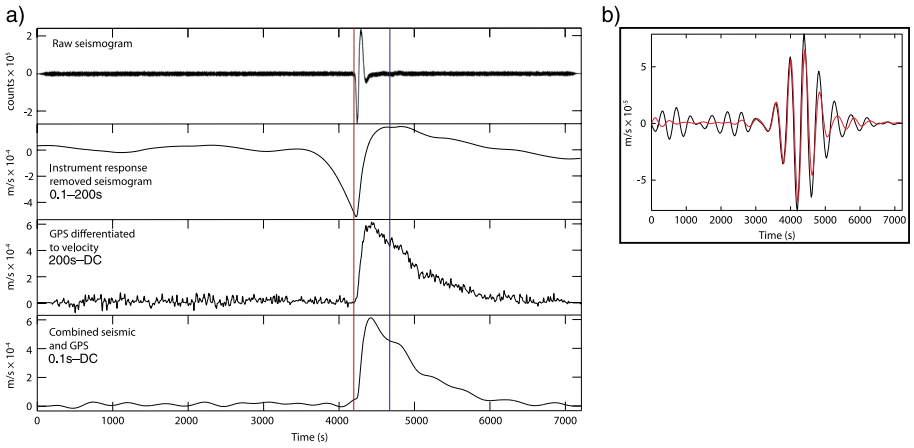

Figure 7. (a) Example of combining GPS and seismic time series. Red and blue vertical lines mark first and second rupture phases, respectively. (b) Comparing seismic and GPS signals in the 300–500 s frequency band: red = seismic, black = GPS.

Rayleigh pulse but not the interevent-locked central asperity? Far-field seismic-wave amplitudes originating from sliding processes, such as during an earthquake and WIS slip events, are controlled by the time derivative of the seismic moment, a measure of the energy released during the event. Thus, in order to explain the waveforms of the teleseismic signal, it is important to completely resolve this moment rate function (MRF) of the fault, defined by the time derivative of the seismic moment function $M(t)$ in N m:

$$M(t) = \mu D(t) S(t) \tag{3}$$

where μ is the shear modulus in pascals, $D(t)$ is the fault displacement in meters, and $S(t)$ is the area of the fault in square meters.

Winberry et al. [2011] constructed MRFs for WIS slip events, but their analysis was hampered due to the fact that GPS records of ice motion have high noise levels in the frequency band of the observed teleseismic signals (20–100 s). However, we now have coverage over most of the ice stream with in situ GPS instruments that resolve the low frequencies (0–0.005 Hz), and seismic sensors that resolve the higher frequencies (0.005–100 Hz) of ice motion. By combining the GPS and seismic time series into a high-fidelity broadband signal of ice motion, we can observe both the high- and low-frequency responses of WIS.

To combine the raw seismic and GPS time series, the instrument response of the seismometer is deconvolved to velocity over a wide bandwidth (0.001–10 Hz). The GPS displacement records are differentiated, and both series are interpolated to a 1 Hz sampling rate (Figure 7). Filtering each colocated record in the period band where seismic and GPS frequencies overlap (e.g., 300–500 s), we see good correlation between the time series in both amplitude and phase (Figure 7b). Two zero-phase filters with 150–500 s linear tapers, high-pass with corner frequency of 150 s for the seismic records, and low-pass with corner frequency of 500 s for the GPS data were applied with the crossover at 325 s. Using these filters to window in the frequency domain, the signals are summed to produce a record containing a complete set of frequencies from 0 to 10 Hz (Figure 7a). This method allows us to remove high-frequency noise observed on the GPS record, while we also are able to record the translational offset of the ice stream motion, which is not possible using only a seismic sensor.

We apply a cubic interpolation between adjacent stations with colocated seismic and GPS instruments to generate a velocity record for the entire ice stream and use this smoothed field to calculate both slip area and displacement. This convolved record is multiplied by the shear modulus of ice (3.5×10^9 N m^{-2}) and differentiated with respect to time to produce the MRF.

Figure 8 shows the MRF calculated from in situ observations during the first two rupture periods, and far-field seismic records for WIS events adjusted for the surface-wave traveltime. Poor on-ice station coverage in the region of the third phase precludes accurate estimation in the later, downstream portion of the rupture and so is not shown. The MRF for the grounding-line initiation point shows a much faster initial increase in moment rate than the MRF for the central initiation point. This results from the much faster rupture velocity (>1 km/s) and expansion of the rupture area for the grounding-line asperity. Filtering the

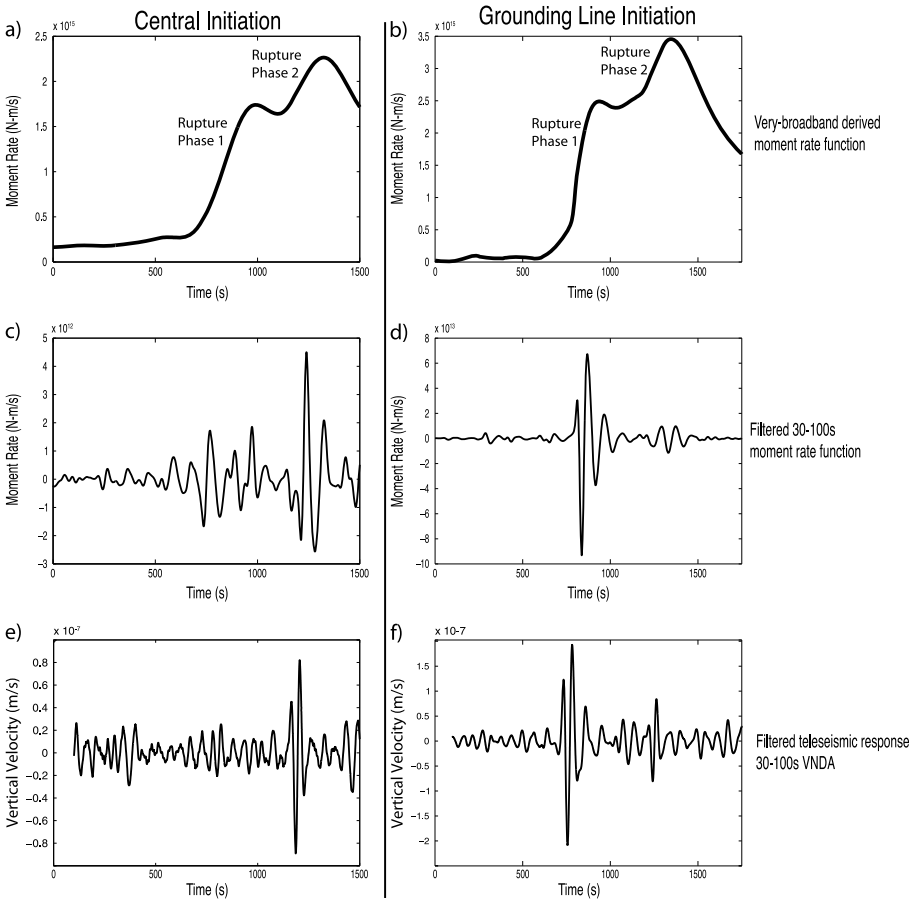

Figure 8. Representative moment rate functions from central and grounding-line initiation events. (a, b) Moment rate functions during the first two phases of WIS slip calculated from the very broadband time series. (c, d) Moment rate functions filtered 30–100 s. (e, f) Teleseismic vertical-component signals filtered 30–100 s from VNDA, traveltime adjusted to align with other figures.

MRFs into the seismic frequency band of 30–100 s shows that the central initiation asperity produces very little radiation at these periods, whereas the grounding-line asperity produces a very strong signal within these periods. Thus, the speed of the initial rupture expansion explains the different far-field responses for the grounding line (first-phase initiation signal) and central initiation points (no first-phase initiation signal). It should be noted that the filtered moment rate functions do not include factors such as the radiation patterns of surface waves and the path response, so we do not expect them to match aspects of the observed waveforms such as polarity.

4.4. Rupture Directivity From Far-Field Seismograms

Further constraints on the initial ruptures originating from the grounding line can be gained from the azimuthal pattern of far-field radiation. Using a subset of the POLENET/ANET deployment throughout West Antarctica with GSN stations QSPA and VNDA, we chose only the highest-amplitude signals: Rayleigh wave arrivals produced by the grounding-line asperity at high tide. The fault surface is approximately horizontal near the Earth's surface, so radiation patterns are the same for both single-force and double-couple solutions: a two-lobe solution [*Ben-Menahem and Singh*, 1981; *Kanamori and Given*, 1982; *Chen et al*., 2011]. The horizontality and shallowness of the fault surface make it relatively inefficient at radiating far-field seismic energy compared to other fault geometries [*Ben-Menahem and Singh*, 1981]. Directivity, rupture propagation close to the velocity of the seismic phase of study, can distort the azimuthal radiation pattern depending on fault length, direction of rupture, and velocity of rupture. The direction of fastest rupture may be in a separate direction to the driving force direction.

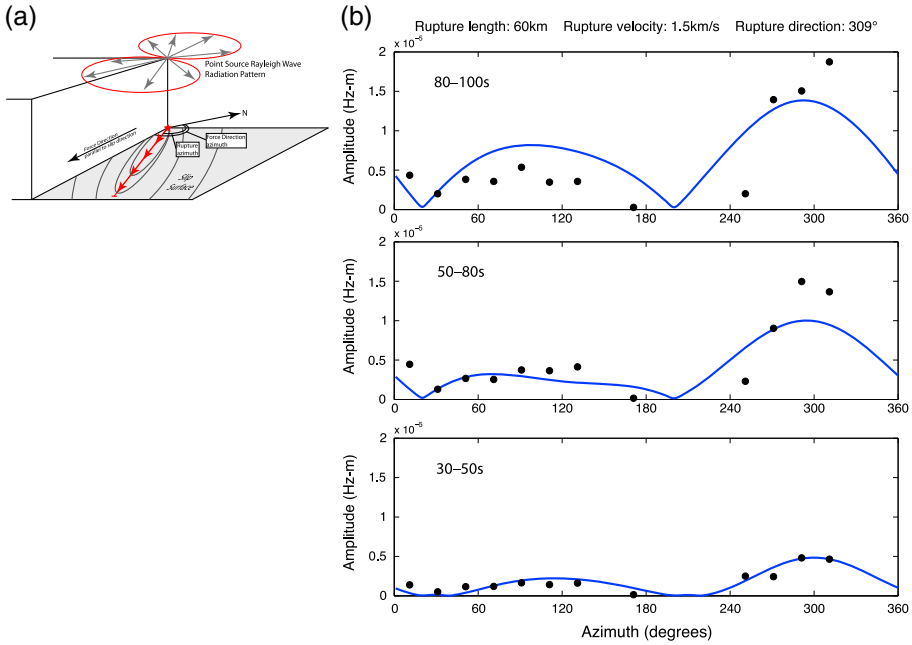

Figure 9. (a) Schematic diagram of directivity parameters. Red star shows initiation point, ellipses on the slip surface are isochrones of the rupture front, red arrowed line shows direction of modeled line source which is not necessarily in the direction of slip. (b) Directivity of grounding-line initiation over three spectral bands with respect to the azimuth of the station to the source. Black points: spectral amplitudes of stations recording WIS first-phase events initiating at high tide at the grounding-line spot. Blue line: best-fit least-squares model result for a fault dipping at 1° and a single force in the direction of 290°.

Stations VNDA and FISH near Ross Island show strong amplitudes, whereas relatively low amplitudes are observed in the many parts of the West Antarctic Ice Sheet. In addition, the signals are much stronger at 80–100 s than at 30–50 s, providing constraints on the duration of the initial rupture. The strongest amplitudes are observed in the downstream direction, suggesting that there is directivity caused by source rupture propagation at velocities close to the shear velocity of the medium [*Ben-Menahem and Singh*, 1981].

We use windowed time series of expected arrival times based on a Rayleigh wave velocity of 3.325 km/s. Spectral amplitude is recorded at bandwidths of 100–80, 80–50, and 50–30 s. Corrections for attenuation and geometric spreading at angular frequency ω were applied to equalize the data at 1000 km:

$$A(\omega, \phi) = A_\Delta e^{\omega\varphi/2QU}\sqrt{\frac{\sin(\Delta)}{\sin(\delta)}} \tag{4a}$$

$$\phi = (\Delta - \delta)\frac{180}{\pi} \tag{4b}$$

where A_Δ is the uncorrected amplitude at a station's angular distance Δ from the source, δ is the angular equalization distance to which all data are corrected, and Q and U are the effective inverse attenuation and group velocity in km/s, respectively, given by the Preliminary Reference Earth Model [*Dziewonski and Anderson*, 1981] at 200 s period [*Chen et al.*, 2011].

A single-force model [*Kanamori and Given*, 1982] with a force direction in the direction of ice flow (290°) is used to attempt an estimation of the rupture velocity and rupture length, using a finite moving line source model [*Ben-Menahem*, 1961] to calculate a source finiteness factor $f(\phi)$:

$$f = \frac{\sin\left[\frac{\omega L}{2v_r}\left(1 - \frac{v_r}{c}\cos\phi\right)\right]}{\frac{\omega L}{2v_r}\left(1 - \frac{v_r}{c}\cos\phi\right)} \tag{5}$$

where, L and v_r are the rupture length and velocity, respectively; c is the phase velocity, and φ is the direction azimuth of the propagating source. The source finiteness factor that contains the propagating fault parameters is then multiplied to the modeled amplitude radiation pattern of a horizontal single-force source (Figure 9).

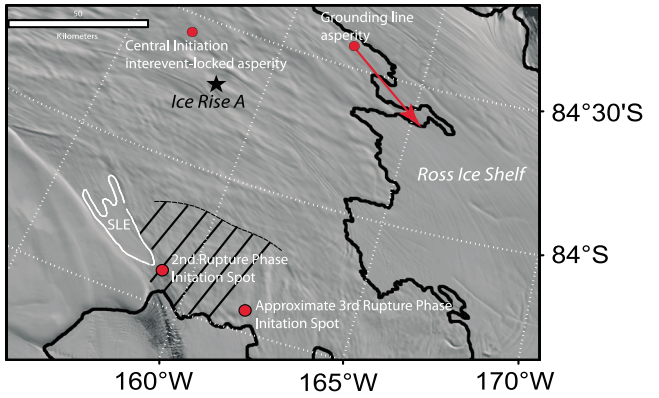

Figure 10. Summary map showing proximity of seismicity-generating areas to grounding line. For the grounding-line initiation the length and direction of rupture determined by the directivity analysis is marked (red arrow). Lined region denotes part of the ice stream where first motion is after the second rupture phase has initiated; this region does not observe the first rupture propagation. SLE = Subglacial Lake Engelhardt. Black line = grounding line from MODIS MOA [*Scambos et al*., 2007].

The location of the grounding-line rupture origin point from the in situ analysis relative to the ice stream extent limits the length of the seismogenic region to <60 km (Figure 10). Observed rupture velocities between stations recording the first responses of slip suggest an initial rupture velocity higher than 1 km/s. We find the best fitting solution to the spectral amplitudes using a grid search over rupture velocity, rupture direction, and source length.

The minimum residual solution over the 30 to 100 s bandwidth, with station amplitudes averaged over 20° intervals, gives a rupture velocity of 1.5 km/s, a rupture length of 60 km, and rupture direction of 309° (Figure 9), which is subparallel to the WIS flow direction. A 60 km rupture length is the upper limit length variable input to the model, determined by a reasonable estimate of grounded ice available in the region. Energetic far-field Rayleigh wave arrival from the grounding-line initial source is produced by relatively rapid rupture (1.5 km/s) in the initial 40 s of the slip event in a direction 19° northward of the direction of ice flow.

5. Discussion

Coupled analysis of both on-ice and teleseismic signals has allowed us to locate the regions of WIS radiating teleseismic energy and to better understand variability in seismic amplitudes. The source regions for all of the observed far-field Rayleigh wave arrivals are asperities in close proximity to the grounding zone (Figure 10). These asperities are loci of fast rupture propagation and rupture zone expansion that generate sudden increases in the moment rate function, producing the observed teleseismic radiation of elastic surface waves. These regions are not associated with the maximum ice displacement or peak slip velocities during a slip event. This is demonstrated conclusively for the initial grounding-line slipping asperity, which shows an initial rupture velocity much faster (1.5 km/s) than the average velocity for the entire slip event (150 m/s). We interpret these observations in the context of the asperity model for earthquake slip, where regions of higher friction show stronger seismic radiation due to larger slip and faster rupture propagation [*Lay and Kanamori*, 1981; *Rice*, 1993]. This suggests that the WIS grounding line is characterized by higher friction than the corresponding upstream areas.

The increased instrumental coverage on the stick-slip portion of WIS in our study allows observation of variations in rupture velocity during slip, providing direct linkage between observations on WIS and the far-field seismic signals. It is also possible to track the rupture front, the points at which the ice stream accelerates, throughout the slip phase and observe any subsequent accelerations as a result of more resistant regions of the bed.

This inference of a strong grounding zone is consistent with an emerging body of evidence from WIS and surrounding areas. *Horgan and Anandakrishnan* [2006] found long-term stability of the grounding-zone location despite the known nonsteadiness of flow. The grounding-zone sedimentary wedge detected by *Anandakrishnan et al*. [2007] provides some stabilization topographically [*Alley et al*., 2007]. Tidally driven flexure extending a few kilometers inland is expected to compact subglacial till, strengthening it [*Walker et al*., 2013], and the pattern of surface slope and deformation of internal radar layers observed in radar and GPS surveys across the grounding zone are consistent with that modeled strong zone [*Christianson et al*., 2013].

The first phase of fast rupture and ice stream acceleration initiates at one of two separate regions. The interevent-locked central initiation asperity is located near the upstream part of the stick-slip region. This

spot is not located beneath Ice Rise A as originally thought [e.g., *Wiens et al*., 2008] but 25 km upstream of this topographical feature. This suggests that the reason for this "sticky" patch is more likely to be associated with geological or hydrological control, perhaps with a local absence of deformable till or a locally drained region [*Stokes et al*., 2007]. The lack of high rupture speeds at the central asperity may be related to the fact that it is surrounded by completely grounded ice that inhibits high-speed rupture.

The grounding-zone initiation asperity is located on the southern edge of WIS. The increase in moment rate from the grounding zone is much faster even with lower maximum moment release than that during a centrally initiated event, resulting in the generation of seismic signals observed at teleseismic distances. Additionally, the directivity of the far-field seismic amplitudes indicates that the first slip phases associated with the grounding zone begin with fast rupture (~1.5 km/s) along a 60 km region subparallel to, and very close to, the grounding zone (Figure 9).

The second rupture motion (8–10 min after first-phase onset) initiates at the northern edge of WIS, confirmed by both the in situ and far-field locations, at the downstream end of Subglacial Lake Engelhardt. The ice to the south of this location remains stationary during first-phase motion, suggesting a strong ice-bed interface. *Winberry et al*. [2011] calculated the hydraulic potential surface in this region to be relatively high compared to other basal regions of WIS, implying that the subglacial till in this region is well drained. Nearby Subglacial Lake Engelhardt provides a frictionless surface allowing rupture to propagate elastically across its length and concentrating stress at its downstream end. Sufficient water is likely to persist to facilitate this propagation even following lake drainage events [*Fricker and Scambos*, 2009].

The third rupture phase, occurring 6–12 min after the second [*Wiens et al*., 2008], is not a stopping phase but instead is identified as a final acceleration of the downstream part of WIS in a region with a relatively complex grounding zone (Figure 10) [*Brunt et al*., 2010]. Both the 2010 and 2011 arrays sampled this acceleration poorly, so an accurate source location of the third phase is not well constrained by our in situ and far-field locations. The cause of this acceleration observed upstream of the potential location is likely the breaking of an additional asperity. This third acceleration phase, like the second rupture phase, causes some upstream regions to increase in velocity.

We find features of the rupture dynamics of WIS that are comparable to, but are much easier to observe than, the complex faulting observed during earthquakes. The WIS rupture develops much slower than typical tectonic earthquakes; the total duration is ~30 min or less and can be observed geodetically. The WIS rupture velocities are ~0.8 times the shear velocity in ice (1.8 km/s) at least shortly after the first and second rupture onsets, in agreement with predictions from rupture mechanics [e.g., *Kanamori and Brodsky*, 2004]. Between the major rupture episodes, the rupture velocity slows to about 150 m/s, perhaps indicating a different mechanical rupture mode away from the high-stress asperities. Pulsed rupture is observed as a healing front that follows the rupture front [*Brune*, 1970], consistent with low-stress state regimes [*Zheng and Rice*, 1998]. Complex rupture involving back-propagation [e.g., *Gabriel et al*., 2012] is also directly observed; the entirety of WIS does not slip concurrently, but regions slip one after another (second- and third-phase motion). Secondary accelerations affect slip velocities in already ruptured regions that are undergoing healing, either increasing their velocity or reducing their deceleration. In this case, velocity functions are asymmetrical where the healing front is much slower than the rupture.

6. Conclusions

We have been able to accurately locate the onset of the first two phases of WIS slip using beamforming techniques and to monitor rupture propagation using seismometers and GPS placed directly on the ice stream. Initial onset of slip occurs from one of two locations, depending on recurrence interval and tidal height. Rupture propagates initially close to the shear wave velocity causing directivity in teleseismic radiation, before decelerating to $<$1 km/s. The second phase of WIS acceleration initiates from the downstream end of Subglacial Lake Engelhardt and from a point not directly influenced by the first phase, reaccelerating fast slip of WIS. The final, third phase of WIS acceleration is not well constrained by our data, although it particularly affects the farthest downstream regions of WIS and could be the acceleration of the rupture out onto the Ross Ice Shelf. Each of the three asperities that produce far-field seismic radiation is located close to or in the grounding zone, suggesting that these regions can support high shear stresses and display fast rupture expansion when the yield stress is exceeded.

WIS slip events are in many ways similar to long-duration earthquakes. Motion between rupture events is retarded in high-friction regions, causing stress to build up. When these asperities break, rupture propagates with varying velocity and seismic energy is released. Being able to place geophysical equipment directly above a regularly slipping fault is a unique opportunity allowing us to study earthquake-like properties in slow motion, a rare occurrence in seismology. In this case the geology is simple compared to earthquake shear zones, and instrumentation can be placed directly above the fault surface without cultural interference. However, differences to natural earthquakes lie in the material properties of the fault zone. Freezing-on at the ice-bed interface likely occurs between slips [*Winberry et al*., 2009], and driving stresses are small, with the system being highly sensitive to small stress fluctuations caused by ice flexure.

We are now able to understand and interpret the far-field observations in terms of the spatial variation in WIS bed properties and their effect on the slip events. Distant seismic observations thus allow a long and consistent time series of WIS slip event characteristics, thus providing a valuable dataset to study the deceleration and presumed stagnation of the WIS.

Acknowledgments

Thanks go to Alex Brisbourne, Peter Burkett, Angela Hoffer, Randy Justin, Tarun Luthra, and Stephanie Kay for help with data collection. We also thank Rick Aster, Audrey Huerta, Andy Nyblade, Terry Wilson, and the rest of the POLENET group for allowing access to seismic data collected during concurrent field seasons. Instrumentation and support was provided by UNAVCO and PASSCAL instrument centers. Raytheon Polar Services, The New York Air National Guard, and Kenn Borek Air provided logistical support. Comments by Fabian Walter, Victor Tsai, and an anonymous reviewer greatly improved this paper. This work was supported by the U.S. National Science Foundation Office of Polar Programs grants ANT-0944671 and ANT-0944794.

References

Alley, R. B. (1993), In search of ice-stream sticky-spots, *J. Glaciol.*, *39*, 447–454.

Alley, R. B., S. Anandakrishnan, T. K. Dupont, B. R. Parziek, and D. Pollard (2007), Effect on ice-sheet grounding-line stability, *Science*, *315*, 1838–1841.

Anandakrishnan, S., and C. R. Bentley (1993), Microearthquakes beneath ice streams B & C, West Antarctica: Observations and implication, *J. Glaciol.*, *39*, 455–462.

Anandakrishnan, S., G. A. Catania, R. B. Alley, and H. J. Horgan (2007), Discovery of till deposition at the grounding line of Whillans Ice Stream, *Science*, *315*, 1835–1838.

Ben-Menahem, A. (1961), Radiation of seismic surface-waves from finite moving sources, *Bull. Seismol. Soc. Am.*, *51*, 401–435.

Ben-Menahem, A., and S. J. Singh (1981), *Seismic Waves and Sources*, Springer, New York.

Bennet, M. R. (2003), Ice streams as the arteries of an ice sheet: Their mechanics, stability and significance, *Earth Sci. Rev.*, *61*, 309–339.

Bindschadler, R. A., M. A. King, R. B. Alley, S. Anandakrishnan, and L. Padman (2003), Tidally controlled stick–slip discharge of a West Antarctic ice stream, *Science*, *301*, 1087–1089.

Blankenship, D. D., S. Anandakrishnan, J. L. Kempf, and C. R. Bentley (1987), Microearthquakes under and alongside ice stream B, Antarctica, detected by a new passive seismic array, *Ann. Glaciol.*, *9*, 30–34.

Brune, J. N. (1970), Tectonic stress and the spectra of seismic shear waves from earthquakes, *J. Geophys. Res.*, *75*, 4997–5009.

Brunt, K. M., H. A. Fricker, L. Padman, T. A. Scambos, and S. O'Neel (2010), Mapping the grounding zone of the Ross Ice Shelf, Antarctica using ICESat laser altimetry, *Ann. Glaciol.*, *51*, 71–79.

Chen, J. L., C. R. Wilson, D. D. Blankenship, and B. D. Tapley (2009), Accelerated Antarctic ice loss from satellite gravity measurements, *Nat. Geosci.*, *2*, 859–862.

Chen, X., P. M. Shearer, F. Walter, and H. A. Fricker (2011), Seventeen Antarctic seismic events detected by global surface waves and a possible link to calving events from satellite images, *J. Geophys. Res.*, *116*, B06311, doi:10.1029/2011JB00862.

Christianson, K., B. R. Parziaek, R. B. Alley, H. J. Horgan, R. W. Jacobel, S. Anandakrishnan, B. A. Keisling, and B. D. Craig (2013), Ice sheet grounding zone stabilization due to till compaction, *Geophys. Res. Lett.*, *40*, 5406–5411, doi:10.1002/2013GL057447.

Clarke, G. K. C. (2005), Subglacial processes, *Annu. Rev. Earth Planet. Sci.*, *33*, 247–276.

Das, S., and K. Aki (1977), A numerical study of two-dimensional rupture propagation, *Geophys. J. Int.*, *50*, 643–648.

Dziewonski, A. M., and D. L. Anderson (1981), Preliminary reference Earth model, *Phys. Earth Planet. Int.*, *25*(4), 297–356.

Ekström, G., M. Nettles, and G. A. Abers (2003), Glacial earthquakes, *Science*, *302*(5645), 622–624.

Fricker, H. A., and T. A. Scambos (2009), Connected subglacial lake activity on lower Mercer and Whillans Ice Streams, West Antarctica, 2003–2008, *J. Glaciol.*, *55*, 303–315.

Gabriel, A.-A., J.-P. Ampuero, L. A. Dalguer, and P. M. Mai (2012), The transition of dynamic rupture styles in elastic media under velocity-weakening friction, *J. Geophys. Res.*, *117*, B09311, doi:10.1029/2012JB009468.

Horgan, H. J., and S. Anandakrishnan (2006), Static grounding lines and dynamic ice streams: Evidence from the Siple Coast, West Antarctica, *Geophys. Res. Lett.*, *33*, L18502, doi:10.1029/2006GL027091.

Hulbe, C., and M. Fahnestock (2007), Century-scale discharge stagnation and reactivation of the Ross ice streams, West Antarctica, *J. Geophys. Res.*, *112*, F03S27, doi:10.1029/2006JF000603.

Joughin, I., and S. Tulaczyk (2002), Positive mass balance of the Ross Ice Streams, West Antarctica, *Science*, *295*, 476–480.

Joughin, I., et al. (2005), Continued deceleration of the Whillans Ice Stream, West Antarctica, *Geophys. Res. Lett.*, *32*, L22501, doi:10.1029/2005GL024319.

Kanamori, H., and E. E. Brodsky (2004), The physics of earthquakes, *Rep. Prog. Phys.*, *67*, 1429–1496.

Kanamori, H., and J. W. Given (1982), Analysis of long-period seismic waves excited by the May 18, 1980 eruption of Mount St. Helens—A terrestrial monopole?, *J. Geophys. Res.*, *87*, 5422–5432.

Lay, T., and H. Kanamori (1981), An asperity model of large earthquake sequences, in *Earth Prediction: An International Review*, *Maurice Ewing Ser.*, vol. 4, edited by D. W. Simpson and P. G. Richards, pp. 579–592, AGU, Washington, D. C.

Lay, T., and T. Wallace (1995), *Modern Global Seismology*, Academic Press, San Diego.

Nettles, M., and G. Ekström (2010), Glacial earthquakes in Greenland and Antarctica, *Annu. Rev. Earth Planet. Sci.*, *38*, 467–491.

Pritchard, H. D., R. J. Arthern, D. G. Vaughan, and L. A. Edwards (2009), Extensive dynamic thinning on the margins of the Greenland and Antarctic ice sheets, *Nature*, *461*, 971–975.

Rice, J. R. (1993), Spatiotemporal complexity of slip on a fault, *J. Geophys. Res.*, *98*, 9885–9907.

Rost, S., and C. Thomas (2002), Array seismology: Methods and applications, *Rev. Geophys.*, *40*(31008), doi:10.1029/2000RG000100.

Scambos, T. A., T. M. Haran, M. A. Fahnstock, T. H. Painter, and J. Bohlander (2007), MODIS-based mosaic of Antarctica (MOA) data sets: Continent-wide surface morphology and snow grain size, *Remote Sens. Environ.*, *111*, 242–257.

Sergienko, O. V., and C. Hulbe (2011), 'Sticky spots' and subglacial lakes under ice streams of the Siple Coast, Antarctica, *Ann. Glaciol.*, *52*, 18–22.
Stokes, C. R., C. D. Clark, O. B. Lian, and S. Tulaczyk (2007), Ice stream sticky spots: A review of their identification and influence beneath contemporary and palaeo-ice streams, *Earth Sci. Rev.*, *81*, 217–249.
Walker, R. T., B. R. Parizek, R. B. Alley, S. Anandakrishnan, K. L. Riverman, and K. Christianson (2013), Ice-shelf tidal flexure and subglacial pressure variations, *Earth Planet. Sci. Lett.*, *361*, 422–428.
Walter, J. I., E. E. Brodsky, S. Tulaczyk, S. Y. Schwartz, and R. Pettersson (2011), Transient slip events from near-field seismic and geodetic data on a glacier fault, Whillans Ice Plain, West Antarctica, *J. Geophys. Res.*, *116*, F01021, doi:10.1029/2010JF001754.
Wiens, D. A., S. Anandakrishnan, J. P. Winberry, and M. A. King (2008), Simultaneous teleseismic and geodetic observations of the stick–slip motion of an Antarctic ice stream, *Nature*, *453*, 770–774.
Wilson, T. J., et al. (2010), The Antarctic POLENET project: Status, initial results, future challenges, AGU Fall Meeting, Abstract GC11A-08.
Winberry, J. P., S. Anandakrishnan, R. B. Alley, R. A. Bindschadler, and M. A. King (2009), Basal mechanics of ice streams: Insights from the stick–slip motion of Whillans Ice Stream, West Antarctica, *J. Geophys. Res.*, *114*, F01016, doi:10.1029/2008JF001035.
Winberry, J. P., S. Anandakrishnan, D. A. Wiens, R. B. Alley, and K. Christianson (2011), Dynamics of stick–slip motion, Whillans Ice Stream, Antarctica, *Earth Planet. Sci. Lett.*, *305*, 283–289.
Winberry, J. P., S. Anandakrishnan, D. A. Wiens, and R. B. Alley (2013a), Nucleation and seismic tremor associated with the glacial earthquakes of Whillans Ice Stream, Antarctica, *Geophys. Res. Lett.*, *40*, 312–315, doi:10.1002/grl.50130.
Winberry, J. P., S. Anandakrishnan, R. B. Alley and D. A. Wiens (2013b), Tidal pacing, stick slip and the slow down of the Whillans Ice Stream. Twentieth West Antarctic Ice Sheet Workshop, Abstract ftp://sidads.colorado.edu/pub/projects/waisworkshop/2013/abstracts/Winberry.pdf.
Zheng, G., and J. R. Rice (1998), Conditions under which velocity-weakening friction allows self-healing versus a cracklike mode of rupture, *Bull. Seismol. Soc. Am.*, *88*, 1466–1483.
Zoet, L. K., S. Anandakrishnan, R. B. Alley, A. A. Nyblade, and D. A. Wiens (2012a), Motion of an Antarctic glacier by repeated tidally modulated earthquakes, *Nat. Geosci.*, *5*, 623–626.
Zoet, L. K., R. B. Alley, S. Anandakrishnan, and K. Christianson (2012b), Accelerated subglacial erosion in response to stick-slip motion, *Geology*, *41*, 159–162.